Research Square

Preprints are preliminary reports that have not undergone peer review.
They should not be considered conclusive, used to inform clinical practice,
or referenced by the media as validated information.

On efficient oxygen evolution reaction: Facile one-pot synthesis of ultra-thin defect rich Pd metallenes

Chaudhry Muhammad Subhan
Pir Mehr Ali Shah Arid Agriculture University
Meysam Amini
m.amini@unsw.edu.au

UNSW Sydney
Dilawar Hassan
University of South Africa
Muhammad Humza Javed
University of Calgary

Article

Keywords: Electrocatalyst, Water splitting, Electrochemical oxidation, Oxygen evolution reaction, Defect-rich palladium metallene

Posted Date: May 7th, 2026

DOI: https://doi.org/10.21203/rs.3.rs-9168120/v1

License: This work is licensed under a Creative Commons Attribution 4.0 International License.
Read Full License

Additional Declarations: No competing interests reported.

Abstract

An effective water-splitting electrocatalyst should be inexpensive, abundant, efficient, stable, and durable; however, the anodic oxygen evolution reaction (OER) remains challenging due to its complex mechanism, slow kinetics, and high energy demand. In this study, defect-rich Pd metallenes were synthesised via a simple one-pot method and evaluated as efficient OER electrocatalysts. Their structural, morphological, and elemental properties were characterised using HRTEM, XRD, and XPS. Electrochemical measurements were conducted in alkaline electrolyte. The defect-rich Pd metallenes exhibited an OER overpotential of 1.62 V, lower than that of commercial Pd/C (1.69 V) at a current density of 10 mA cm^{-2}. They also showed a reduced Tafel slope of 90 mV dec^{-1}, indicating enhanced reaction kinetics. Furthermore, the catalyst demonstrated excellent durability and operational stability. These results highlight the role of defect engineering in improving Pd metallene OER performance and emphasize its potential for sustainable energy applications.

1. Introduction

The oxygen evolution reaction (OER) is a crucial anodic half-reaction in various emerging electrochemical energy conversion landscapes, including water electrolysis, metal–air batteries, photoelectrochemical (PEC) cells, and rechargeable fuel cells [1–3]. Furthermore, OER is essential for the sustainable production of green hydrogen, which is an energy carrier that is expected to be important in the future carbon-neutral fuel economy [4, 5]. By enabling the efficient water splitting into hydrogen and oxygen [6], OER is primarily correlated to the scalability and energy efficiency of hydrogen-powered energy systems [7, 8].

The intrinsically slow kinetics of the OER process make the practical implementation of water electrolysis and other OER-driven technologies extremely challenging [2, 9]. The reaction happens in four steps, and during these steps, high-energy intermediates (*OH, *O, and *OOH) cause big overpotentials. To overcome this kinetic barrier, it is essential to develop robust, efficient, and cost-effective electrocatalysts that will reduce energy requirements and enhance overall system performance [6, 10–12].

At present, IrO_2 and RuO_2 have exhibited the most superior OER performance in acidic conditions [13–15]. However, their high cost, limited availability, and poor long-term durability hinder large-scale utilisation [16–18]. Consequently, there is a pressing demand for alternative catalysts that exhibit high OER activity, demonstrate electrochemical stability, and minimise dependency on scarce noble metals [19–21]. Palladium (Pd), a member of the platinum group of metals, has garnered significant attention due to its favourable d-band structure, greater abundance compared to Pt and Ir, and the ability to modify its surface chemistry [21–24].

Recent studies demonstrate that the electrocatalytic performance of Pd can be significantly enhanced through nanostructuring, alloying, and surface/interface engineering [25–27]. These Pd-based nanomaterials cause high surface-to-volume ratio, reduced diffusion distances for charge carriers, and

optimal exposure of active surface atoms, suitable for catalytic applications [28–30]. Defect engineering has also become an established method for improving the electrical properties and catalytic performance of two-dimensional materials. The emergence of structural defects, including vacancies, grain boundaries, and edge dislocations, can modify the local charge density, produce strain, and shift the d-band centre of Pd atoms [31–34]. This modifies the binding energy of chemical intermediates. These effects can collectively reduce the energy barriers that hinder OER phases, especially those related to the synthesis of *O and *OOH, which are generally the most time-consuming steps [35–42].

This study presents the synthesis of Pd-metallenes by using a simple one-pot wet-chemical approach, producing an ultrathin, defect-rich morphology. Transmission electron microscopy (TEM), X-ray diffraction (XRD), and X-ray photoelectron spectroscopy (XPS) were performed to study the structural morphology and electronic properties. Electrocatalytic performance for the OER was performed by linear sweep voltammetry (LSV) in alkaline aqueous media. The Tafel slope was calculated to analyse the reaction kinetics along with the electrochemical impedance measurements (EIS) in the OER region. Furthermore, stability tests were conducted to evaluate the durability of the catalyst under prolonged electrochemical operation.

2. Results and discussion

2.1. Synthesis

Pd (II) acetylacetonate ($Pd(acac)_2$, 99%), molybdenum hexacarbonyl ($Mo(CO)_6$), oleylamine (OAm, 70%), Ethylene glycol (EG, 99.8%), commercial 20 wt % Pd (Pd/C) on graphitized carbon. All chemicals were purchased from Sigma-Aldrich. Deionized water (18.2 MΩ), 5 wt % Nafion 117 solution, ethanol, hexane, and potassium hydroxide (KOH) were used.

Pd metallenes (Pd-m) were synthesised using a standard solution-phase reduction method. For this process, 10 mg of $Pd(acac)_2$, 30 mg of ascorbic acid, 4 mg of $Mo(CO)_6$ and 5 ml of OAm were added in a 20 ml glass vial and ultrasonicated for 1 h to obtain a homogenous solution. The vial was then sealed and placed in a silicon oil-based bath at 80°C for 7 hours. After cooling down to room temperature, the colloidal product was collected using centrifugation and washed three times with ethanol and hexane mixture to remove excess OAm. After washing, the final product of Pd-m was then dispersed in ethanol for electrochemical measurements [42]. For the preparation of the catalyst ink, 5 mg of metallenes and Pd/C were dispersed in 1 mL of solution containing ethanol, Nafion and water. Then the mixture was sonicated for 1 hour in an ice bath to ensure uniform dispersion. After sonication, the solution was uniformly deposited onto carbon paper foam using a spray gun, to form a homogeneous catalyst layer. The coated electrode was subsequently dried and ready for further electrochemical measurements.

2.2. Characterisations

The morphology and microstructural characteristics of the synthesised catalysts were investigated using high-resolution TEM (HRTEM), high-angle annular dark-field scanning transmission electron

microscopy (HAADF-STEM), and energy-dispersive X-ray spectroscopy (EDS) elemental mapping. TEM analyses were performed on a JEOL JEM-ARM300F2 instrument, an aberration-corrected scanning/transmission electron microscope (AC-STEM) equipped with a cold field-emission gun, providing atomic-resolution imaging and precise elemental analysis. The crystal structure of the catalysts was analysed using an XRD instrument (PANalytical Empyrean) equipped with Cu Kα radiation (λ = 1.5406 Å). XPS was performed on a Thermo ESCALAB 250Xi high-resolution spectrometer using a monochromatic Al Kα X-ray source.

Ultrathin defect-rich Pd-m were successfully prepared through a one-pot synthesis approach, as illustrated in Fig. 1a, followed by deposition on carbon paper and testing in a three-electrode setup. The TEM images of Pd-bm, shown in Fig. 1b–c, confirm the successful synthesis of an ultrathin, lamellar structure with a slightly wrinkled morphology. The porous nanosheets contain a high density of defects and exhibit a relatively large specific surface area, which facilitates abundant exposure to catalytically active sites and contributes to their enhanced catalytic performance. Figure 1d–e presents low-magnification TEM images show individual Pd nanosheets. Clear lattice fringes with a d-spacing of 0.228 nm are observed, corresponding to the (111) plane of face-centred cubic centred Pd. As portrayed in Fig. 1f–h, the HAADF-STEM image and the corresponding elemental mapping images reveal a uniform spatial distribution of Pd throughout the catalyst, confirming the successful formation of Pd-bm.

Figure 2a shows low-magnification TEM images highlighting the structural defects in Pd-m, including amorphous regions, semi-amorphous domains, and a significant number of vacancies. The corresponding FFT patterns further confirm the presence of semi-crystalline region. The abundant defects present in nanosheets are expected to play a crucial role in regulating the catalytic performance by providing additional active sites. XRD patterns were recorded to investigate the crystal structures of Pd-m, as shown in Fig. 2b, the diffraction peaks located at 38.1°, 46.7°, and 68.1° can be indexed to the (111), (200), and (220) crystallographic planes of FCC Pd (JCPDS No. 46-1043), respectively [43]. XPS was also performed to investigate the chemical composition and electronic structure of the catalysts. As illustrated in Fig. 2c, the Pd 3d XPS spectrum of Pd-m displays characteristic Pd $3d_{5}/_{2}$ and Pd $3d_{3}/_{2}$ doublets, which can be deconvoluted into two distinct components. The peaks located at 335.0 and 340.3 eV are assigned to metallic Pd^{0}, corresponding to the Pd $3d_{5}/_{2}$ and Pd $3d_{3}/_{2}$ states, respectively. In addition, weaker peaks appearing at 336.3 and 341.8 eV are attributed to Pd^{2+} species, indicating the presence of surface PdO. Figure 2d shows the overall XPS survey spectrum, highlighting the presence of Pd 3d, C 1s, and O 1s peaks [34].

2.3. Electrochemical Measurements

The electrochemical activity was studied in 1 M KOH aqueous solution by using a Multi Autolab M204 electrochemical workstation with a three-electrode configuration equipped with Pt wire as the counter electrode (CE), while an Hg/HgO as the reference electrode (RE). The working electrode (WE) was prepared on carbon fibre paper (CFP) with a selected area of 1 cm × 0.75 cm. All potentials reported were referenced to the reversible hydrogen electrode (RHE) using the following standard Nernst equation:

$E_{RHE} = E_{Hg/HgO} + 0.05916 \times pH + E^{\circ}_{Hg/HgO}$ **Eq. 1**

where, E_{RHE} is the potential vs. RHE, $E_{Hg/HgO}$ is the potential measured vs. Hg/HgO and ($E^{\circ}_{Hg/HgO}$ = 0.098 V) at room temperature. The open circuit potential (OCP) was recorded for 60 seconds prior to each experiment to ensure valid electrical connections before all measurements. The catalyst deposited on CFP was immersed in the electrolyte for 45 minutes to facilitate proper wetting of the catalyst. After wetting, the preconditioning of the electrode was conducted by cyclic voltammetry (CV) (0.25 to 1.1 V vs. V_{RHE} at a scan rate of 20 mV/s) to facilitate the transformation of the as-coated catalyst into its hydroxide/oxyhydroxide species. The catalytic activity for the Tafel analysis was determined using LSV at a scan rate of 5 mV/s.

2.4. Electrocatalytic performance for OER

The electrocatalytic performance of the as-deposited electrodes was evaluated in 1 M KOH using a three-electrode setup for OER measurements. The OER activity was also conducted with a commercially prepared Pd/C electrode. LSV performed in the anodic region, as demonstrated in Fig. 3a, Pd-m required a lower overpotential of 1.62 V to achieve a current density of 10 mA cm^{-2}, outperforming Pd/C (1.69 V). Figure 3b compares the overall potentials of Pd-m and Pd/C electrodes at different current densities, demonstrating that Pd-m exhibits superior OER performance compared to Pd/C. The Tafel slopes were also calculated to further evaluate the OER kinetics, as shown in Fig. 3c. Pd-m exhibits a lower Tafel slope of 90 mV dec^{-1} compared to Pd/C (102 mV dec^{-1}), indicating faster reaction kinetics for Pd-m. Electrochemical impedance spectroscopy (EIS) was performed in the OER region to evaluate the interfacial charge-transfer kinetics of Pd-based catalysts. The Nyquist plots shown in Fig. 3d reveal that Pd-m exhibits the smallest charge-transfer resistance (R_{ct}), indicating faster electron transfer and more favourable reaction kinetics towards the OER.

The electrochemically active surface area (ECSA) was calculated from the double-layer capacitance (C_{dl}) values of both Pd/C and Pd-m, which were obtained from CV measurements conducted in non-faradaic region at different scan rates from 20 to 150 mV within the potential window of 0.92–1.135 V vs. RHE, as highlighted in Fig. 4a and Figure S1. Pd-m exhibits the highest C_{dl} value of 12.3 mF cm^{-2}, as shown in Fig. 4b, which is significantly larger than the commercially prepared Pd electrode (10.3 mF cm^{-2}). Figure 4c further shows that Pd-m exhibits larger oxidation and reduction currents compared to Pd/C, indicating a higher ECSA, which contributes to its enhanced catalytic activity. In the inset of Fig. 4d, a long-term stability test was conducted at a constant current density of 10 mA cm^{-2} to evaluate the durability of the Pd-m catalyst. The results demonstrate excellent operational stability, with the catalyst potential exhibiting a slight shift towards lower values during prolonged operation, indicating favourable catalytic durability and better electrochemical performance for OER.

3. Conclusion

In conclusion, ultra-thin defect-rich Pd-m synthesised via a simple one-pot method demonstrate a superior electrocatalytic performance for the OER in alkaline media. Structural and surface analyses confirm the formation of ultrathin Pd nanosheets with abundant defects, which effectively modify the electronic structure and enhanced catalytic activity. Electrochemical measurements show superior OER kinetics compared to commercial Pd/C, delivering a lower overpotential (1.62 V at 10 mA cm^{-2}) and a smaller Tafel slope (90 mV dec^{-1}). The large ECSA, reduced charge-transfer resistance, and outstanding long-term stability further underscores their performance advantages. Overall, the synergistic effects of the two-dimensional morphology and defect-rich structure enable enhanced activity and durability, offering valuable guidance for the rational design of high-performance noble-metal electrocatalysts for sustainable energy conversion.

Declarations

Declaration of Competing Interest

The authors declare that they have no known competing financial interests or personal relationships that could have appeared to influence the work reported in this paper.

Funding

This research received no external funding.

Author Contribution

CMS: Investigation; Writing article draft MA: Methodology; Conceptualization; Review & editionDH: Investigation; VisualizationMHJ: Investigation; Software

Acknowledgment

The authors gratefully acknowledge the invaluable scientific and technical support provided by PMAS Arid Agriculture University, the University of New South Wales (UNSW), the University of South Africa, and the University of Calgary.

Data Availability

Absolute access to data and supplementary information is granted upon request.

References

1. Fabbri, E. & Schmidt, T. J. *ACS Catal.* **8** 9765–9774. (2018).
2. Favaro, M. et al. *J. Am. Chem. Soc.* **139** 8960–8970. (2017).
3. Jesudass, S. C. et al. *Electrochem. Energy Reviews* **6** 27. (2023).
4. Tahir, M. et al. *Nano Energy* **37** 136–157. (2017).
5. Yang, H., Driess, M. & Menezes, P. W. *Adv. Energy Mater.* **11** 2102074. (2021).
6. You, B. & Sun, Y. *Acc. Chem. Res.* **51** 1571–1580. (2018).
7. Yang, H., Driess, M. & Menezes, P. W. *Adv. Energy Mater.* **11** (2021).
8. Lei, Z. et al. *Nat. Commun.* **13** (2022).
9. Lu, X., Ahmadi, M., Disalvo, F. J. & Abruña, H. D. *ACS Catal.* **10** 5891–5898. (2020).
10. Chen, F. Y., Wu, Z. Y., Adler, Z. & Wang, H. *Joule* **5** 1704–1731. (2021).
11. She, Z. W. et al. Science 355 (2017). (1979).
12. Kou, T., Wang, S. & Li, Y. *ACS Mater. Lett.* **3** 224–234. (2021).
13. Anantharaj, S., Kundu, S. & Noda, S. *Nano Energy* **80** (2021).
14. Chen, Y. et al. *Chem. Rev.* **118** 6409–6455. (2018).
15. McCrory, C. C. L., Jung, S., Peters, J. C. & Jaramillo, T. F. *J. Am. Chem. Soc.* **135** 16977–16987. (2013).
16. Seitz, L. C. et al. A Highly Active and Stable IrO x /SrIrO 3 Catalyst for the Oxygen Evolution Reaction, n.d.
17. Fang, Z. et al. *ACS Nano* **11** 9550–9557. (2017).
18. Shi, Y. et al. *Chem. Rev.* **121** 649–735. (2021).
19. Yu, M., Budiyanto, E. & Tüysüz, H. *Angewandte Chemie - Int. Ed.* **61** (2022).
20. Zhao, Z. & Xia, Z. *ACS Catal.* **6** 1553–1558. (2016).
21. Huang, S. et al. *ACS Nano* **16** 522–532. (2022).
22. Vij, V. et al. *ACS Catal.* **7** 7196–7225. (2017).
23. Yoshino, S., Takayama, T., Yamaguchi, Y., Iwase, A. & Kudo, A. *Acc. Chem. Res.* **55** 966–977. (2022).
24. Trotochaud, L., Young, S. L., Ranney, J. K. & Boettcher, S. W. *J. Am. Chem. Soc.* **136** 6744–6753. (2014).
25. Cheng, H. et al. *Adv. Mater.* **32** (2020).
26. Chen, A. & Ostrom, C. *Chem. Rev.* **115** 11999–12044. (2015).
27. Iqbal, M. et al. *Small* 15 (2019).
28. Wang, T. et al. *Energy Environ. Sci.* **14** 2639–2669. (2021).
29. Bredar, A. R. C., Chown, A. L., Burton, A. R. & Farnum, B. H. *ACS Appl. Energy Mater.* **3** 66–98. (2020).
30. Prabhu, P. & Lee, J. M. *Chem. Soc. Rev.* **50** 6700–6719. (2021).
31. Song, J. et al. *Chem. Soc. Rev.* **49** 2196–2214. (2020).
32. Guo, R. et al. *J. Mater. Chem. Mater.* **9** 6196–6204. (2021).

33. Zhang, J. et al. *Adv. Mater.* **34** (2022).
34. Yu, H. et al. *Angewandte Chemie - Int. Ed.* **60** 12027–12031. (2021).
35. Shi, Y., Lyu, Z., Cao, Z., Xie, M. & Xia, Y. *Angewandte Chemie - Int. Ed.* **59** 19129–19135. (2020).
36. Zhang, J. et al. *ACS Catal.* **10** 8597–8610. (2020).
37. Liu, W. et al. *Angewandte Chemie - Int. Ed.* **51** 5743–5747. (2012).
38. Negahdar, L., Zeng, F., Palkovits, S., Broicher, C. & Palkovits, R. ChemElectroChem 6 5588–5595. (2019).
39. Koper, M. T. M. *J. Electroanal. Chem.* **660** 254–260. (2011).
40. Cheng, R. et al. *Adv. Mater.* **36** (2024).
41. Wang, H. et al. *Chem. Eng. J.* **450** (2022).
42. Cui, H. et al. *ACS Appl. Nano Mater.* **7** 13280–13288. (2024).
43. Gong, Z. et al. *J. Energy Chem.* **91** 637–644. (2024).

Figures

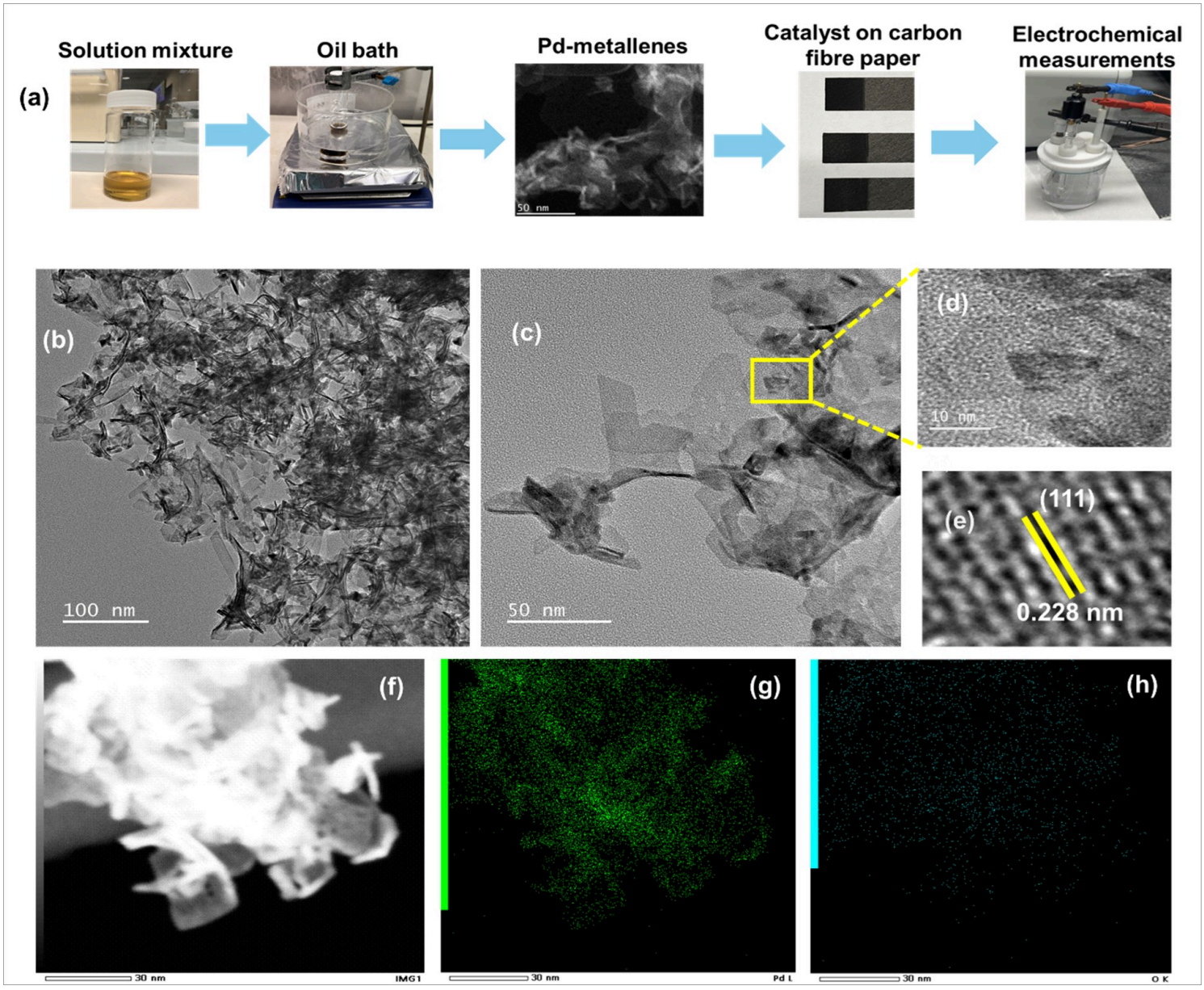


Figure 1

(a) Schematic illustration of synthesis of ultra-thin Pd-m; (b, c) low magnification TEM image (d, e) HRTEM images and illustration of the lattice fringe (f, g, h) high-angle annular dark-field (HAADF) image and corresponding EDS mapping of Pd-bm.

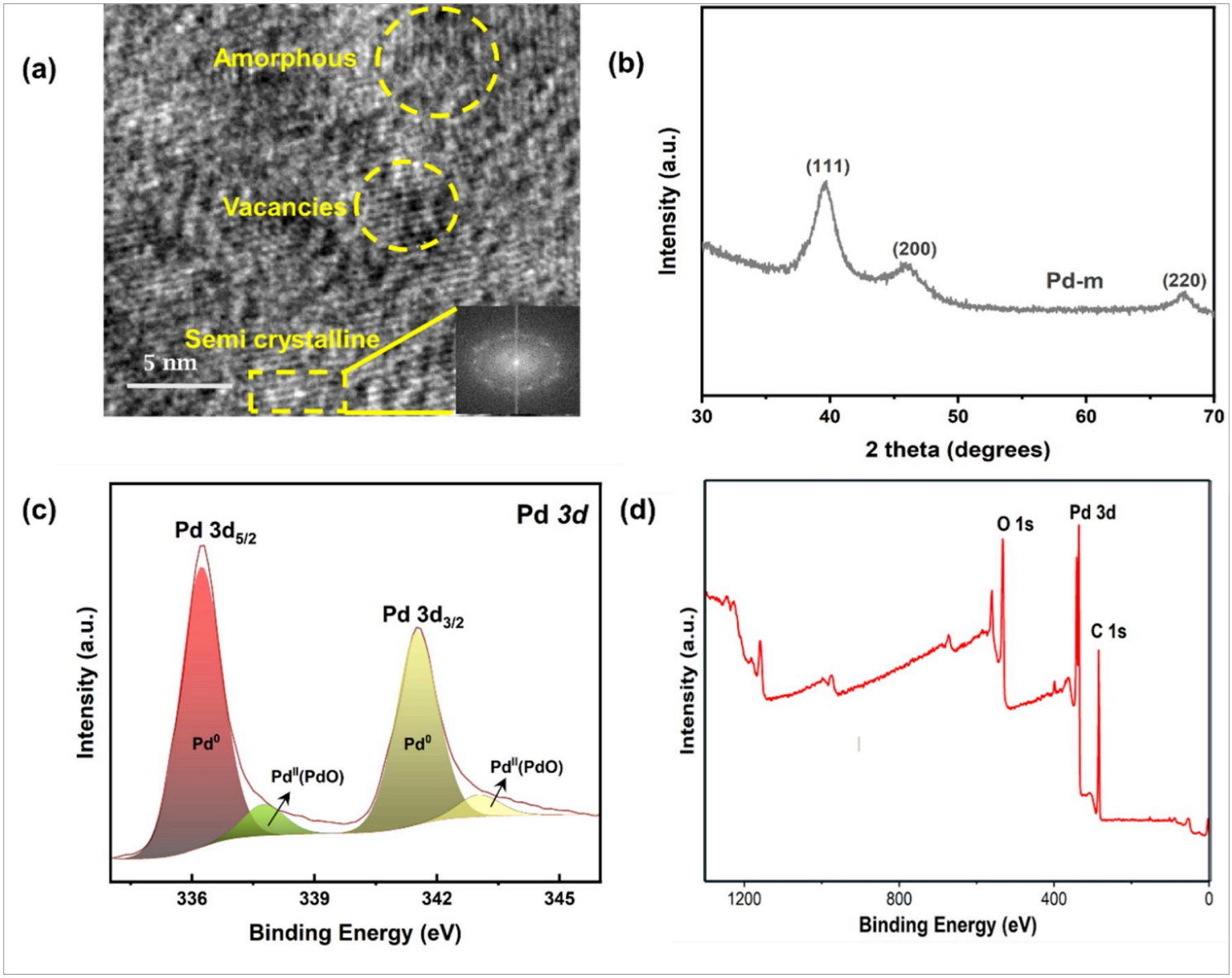


Figure 2

(a) HRTEM images of Pd-m highlighting the material's defects. (b) XRD patterns of synthesised Pd-m. (c) As-synthesised Pd-m Pd 3d XPS spectra (d) XPS survey plot.

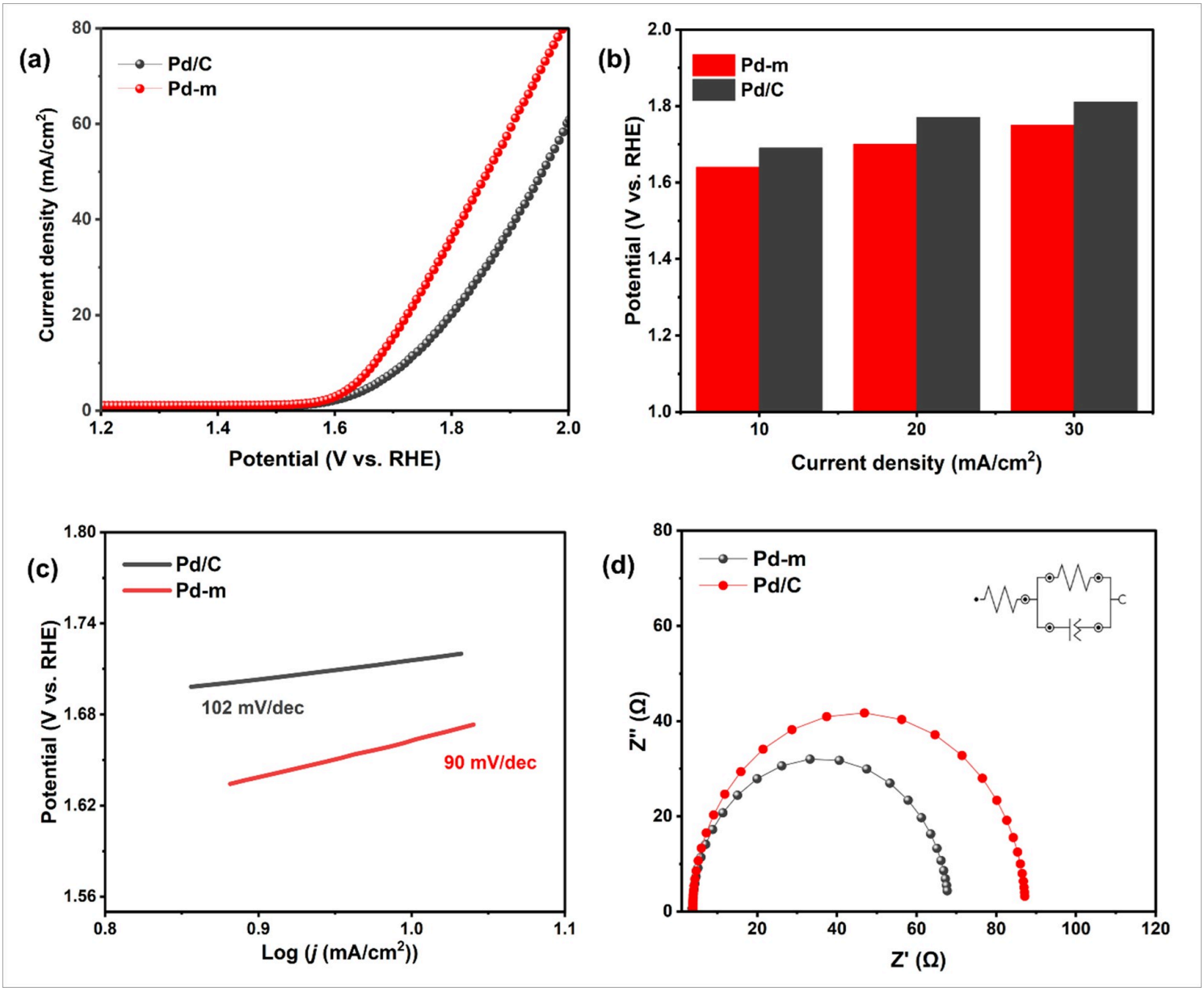


Figure 3

(a) LSV curves of OER (b) OER potentials to achieve at different current densities. (c) Tafel slope values of Pd/C and Pd-m. (d) EIS measurements along with an equivalent circuit diagram.

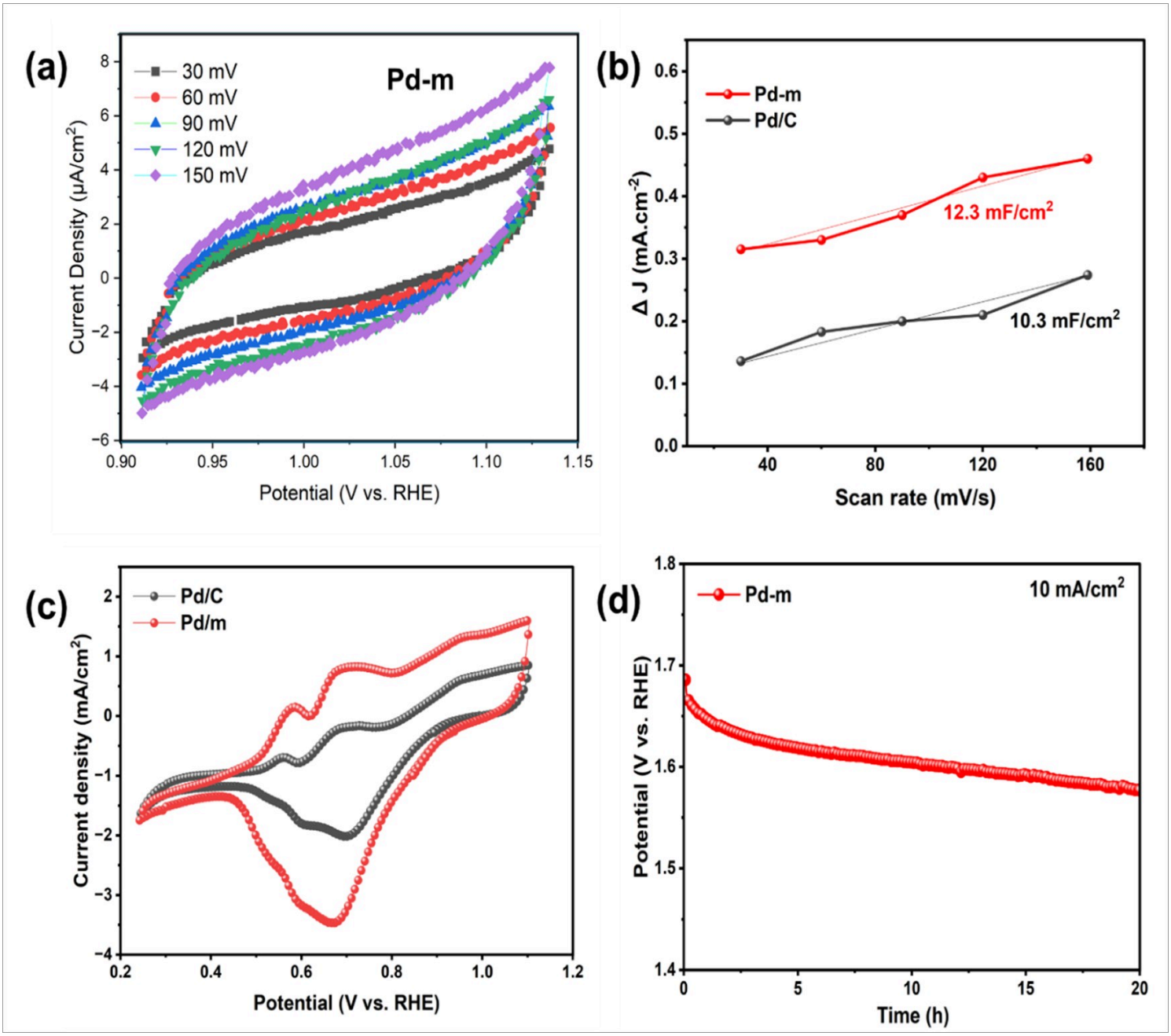


Figure 4

(a) Non-faradaic region CV curves of Pd-m at different scan rates from 30 to 150 mV. (b) The capacitive current 1.02 V as a function of scan rate for different Pd-m catalysts. (c) CV curves for Pd/C and Pd-m. (d) Long-term stability measurements of Pd-m at 10 mA/cm $^{-2}$.

Supplementary Files

This is a list of supplementary files associated with this preprint. Click to download.

- SICMSOER.docx